A 2DOF SOI-MEMS Nanopositioner With Tilted Flexure Bulk Piezoresistive Displacement Sensors

Mohammad Maroufi, *Student Member, IEEE*, and S. O. Reza Moheimani, *Fellow, IEEE*

Abstract—We describe a novel high-bandwidth two degree of freedom microelectromechanical system nanopositioner. On-chip piezoresistive sensors and four electrostatic actuators are incorporated. The bulk piezoresistivity of tilted clamped-guided beams is used to facilitate the fabrication process by eliminating the need for implementing highly doped regions on flexures. To enhance the mechanical characteristics of the nanopositioners, folded springs are also proposed, analytically modeled, and implemented as a component of the device suspension system. The nanopositioner demonstrates a displacement range larger than 15 μm and in-plane resonance modes above 3.6 kHz in both axes. A significant increase in the bandwidth of the piezoresistive sensors is achieved by improving their on-chip signal routing layout. Sensing bandwidths as wide as 55 kHz are experimentally demonstrated for the modified sensors. Characterization reveals a phase response with minimal delay over a large bandwidth, making the device a promising platform for implementation of high-performance feedback control systems. The nanopositioner is also used as the scanning stage of an atomic force microscope for imaging purposes.

Index Terms—MEMS nanopositioner, piezoresistive sensor, feedthrough reduction, folded springs, atomic force microscopy.

I. INTRODUCTION

NANOPOSITIONERS constitute a crucial component of numerous scientific instruments due to their ability to produce displacements with nanometer or sub-nanometer precision. Emergence of state-of-the-art applications such as nanolithography [1], [2], scanning probe microscopy [3], and probe-based data storage systems with ultrahigh density [4], [5] has led to a significant progress in the development of nanopositioners. Research in this field aims to enhance critical features of the nanopositioners including their resolution, displacement range and speed.

The feasibility of using microelectromechanical systems (MEMS) nanopositioners has also been examined in applications such as on-chip atomic force microscopes (AFMs) [6], optical scanners [7], and tunable micro optics [8]. MEMS nanopositioners benefit from the batch

M. Maroufi is with the Department of Mechanical Engineering, University of Texas at Dallas, Richardson, TX 75080 USA (e-mail: mohammad.maroufi@utdallas.edu).

S. O. R. Moheimani was with the School of Electrical Engineering and Computer Science, University of Newcastle, Callaghan, NSW 2308, Australia. He is now with the Department of Mechanical Engineering, University of Texas at Dallas, Richardson, TX 75080 USA (e-mail: reza.moheimani@utdallas.edu).

fabrication capability of the microfabrication processes with the potential to reduce the cost of their production. Silicon, as the prevalent structural material, also provides a relatively high mechanical strength with a low density, which makes higher bandwidths to be achievable by MEMS nanopositioners.

The process of microfabrication, however, imposes certain restrictions on the selection of the sensing and actuation mechanisms for MEMS nanopositioners. Among the actuation mechanisms with microfabrication compatibility, electrothermal actuators provide a relatively high force. However, their high working temperature and sluggish dynamics limit their widespread use in MEMS nanopositioners. Electrostatic actuators, on the other hand, do not pose such restrictions on the speed. The generated force with this actuation method, nevertheless, is comparatively smaller than what may be achieved with electrothermal actuators.

Many of the MEMS nanopositioners reported in the literature do not include on-chip displacement sensors (see e.g. [9]–[12]). Rather, they use off-chip optical sensors for characterization. For on-chip displacement sensing, however, capacitive, electrothermal, and piezoresistive sensors have been successfully incorporated in MEMS nanopositioners. Capacitive sensors typically demonstrate high-resolution performance over a wide bandwidth [13], and their implementation is often compatible with standard microfabrication processes. In [14] and [15], these displacement sensors are implemented in MEMS nanopositioners. In [16], by using a displacement amplification mechanism, position measurement is achieved with sub-nanometer resolution in a 2DOF MEMS nanopositioner. In all these examples, a relatively large fraction of the chip space was allocated to the realization of capacitive sensing elements. This problem can be alleviated in electrostatic MEMS nanopositioners by using the comb-drive actuators simultaneously for sensing and actuation purposes [17], [18]. This, however, requires the implementation of modulation and demodulation techniques, which adds more complexity to the readout circuitry.

Electrothermal sensors operate based on the variation in heat transfer rate between a pair of heaters and a moving stage which serves as a heat sink. The displacement is measured based on the temperature variations and, as a result, opposite resistance changes in the pair of heaters induced by the stage displacement [19]–[21]. The use of these sensors in MEMS nanopositioners is straightforward as they have small form factors and require a relatively simple readout circuitry [6], [22]. As discussed in [6], however, electrothermal sensors show a relatively low bandwidth, which is due to

the involvement of the heat transfer process in their sensing mechanism.

The piezoresistivity of silicon has also been exploited in the MEMS nanopositioners for displacement measurement [23], [24]. This sensing mechanism is based on the variation of the electrical conductivity of silicon when it is mechanically stressed [25]. Piezoresistive sensors offer a wide sensing bandwidth [26], occupy small on-chip space and require a relatively simple readout circuitry. However, extra fabrication efforts are normally needed to incorporate the necessary conducting layers and highly-doped regions on mechanical flexures. These additional steps are not typically available through standard MEMS fabrication processes.

In order to exploit the piezoresistive sensing concept while using a standard microfabrication process, bulk piezoresistivity of mechanical flexures may be used. This concept was implemented for a MEMS resonator in [27]. We also introduced an on-chip displacement sensor in [28] based on the bulk piezoresistivity of silicon flexures. The mechanical and sensing properties of this sensor were also analytically studied in [29]. The electrical resistance variation of two tilted silicon beams due to their bulk piezoresistivity is used in the proposed sensing mechanism for measurement. Implementation of this mechanism eliminates the necessity of using extra fabrication steps to realize highly-doped regions. As demonstrated in [28] and [29], although these sensors display a linear behavior with nanometer resolution, the presence of feedthrough signals limits their achievable bandwidth.

In this work, bulk piezoresistive sensors are incorporated into the design of a 2DOF MEMS nanopositioner. The device is intended to be used as the scanning stage of an AFM. The configuration of the sensors and their on-chip signal routing are modified leading to a dramatic mitigation of the cross-talk between sensing and actuation. Thus, the sensors show significantly wider bandwidths. In order to improve the mechanical characteristics of the nanopositioner, folded springs are also implemented as complementary components of its suspension system. The stiffness of these springs is also modeled using both analytical and finite element approaches.

The remainder of this paper continues as follows. Sec. II details the design and fabrication of the nanopositioner. Here, the stiffness of the proposed folded spring is also modeled. In Sec. III, the configuration of the piezoresistive sensors and their readout circuits are explained. Sec. IV reports the nanopositioner's characterization results. In Sec. V, the improvement of the feedthrough behavior is further discussed. Sec. VI explains AFM imaging where the nanopositioner is used as a scanner, and Sec. VII concludes the paper.

II. NANOPOSITIONER DESIGN AND FABRICATION

The proposed nanopositioner uses parallel kinematic mechanism, allowing the stage to displace along the X and Y directions. Design of one side of the nanopositioner is shown in Fig. 1. The device is symmetrically designed, thus this schematic adequately illustrates its functionality. Nine electrostatic comb-derive structures are incorporated on each side. The mass of these structures is reduced while maintaining their mechanical stiffness through the use of
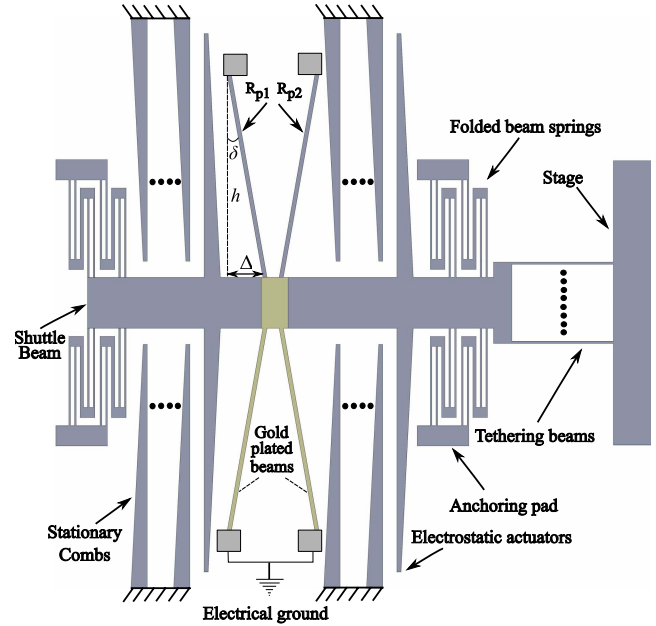

Fig. 1. The schematic of the mechanical design of the nanopositioner in one side along the X direction.

a trapezoidal geometry. The force generated by the actuators is transferred to the stage via a shuttle beam and eight tethering beams.

Two pairs of tilted beams are implemented on each side, anchored on one end and connected to the shuttle beam on the other. These beams simultaneously function as the suspension mechanism and the piezoresistive displacement sensor. The electrical resistances of one pair of these beams are designated by R_{p1} and R_{p2} in Fig. 1, and the other pair is gold-plated and connected to the electrical ground. R_{p1} and R_{p2} undergo opposite variations with shuttle beam displacement. This change in resistance is used as the sensing signal [29]. To complete the suspension system, eight folded springs are implemented on all sides of the nanopositioner. The design of folded springs and the piezoresistive sensors are further explained in Sec. II-A and Sec. III, respectively.

The device is fabricated using the standard SOIMUMPs microfabrication process [30]. The process starts with a silicon-on-insulator wafer with $25\,\mu m$ thick n-doped single crystal silicon as the device layer. As schematically shown in Fig. 2, a compound layer of gold and chromium with a thickness of $520\,nm$ is initially deposited and patterned for electrical routing. The device layer is then patterned to obtain the main structure of the device using deep reactive ion etching (DRIE). From the back side of the wafer, a combination of reactive ion etching (RIE) and DRIE are used for patterning the $400\,\mu m$-thick substrate. Finally, the device is released by etching the buried oxide layer using the wet etch process.

A scanning electron microscope (SEM) image of the fabricated nanopositioner is shown in Fig. 3. The stage has dimensions of $1.8\,mm \times 1.8\,mm$. Square-shaped gold features are also fabricated on the stage as shown in the close-up view. These features are later used as reference patterns during
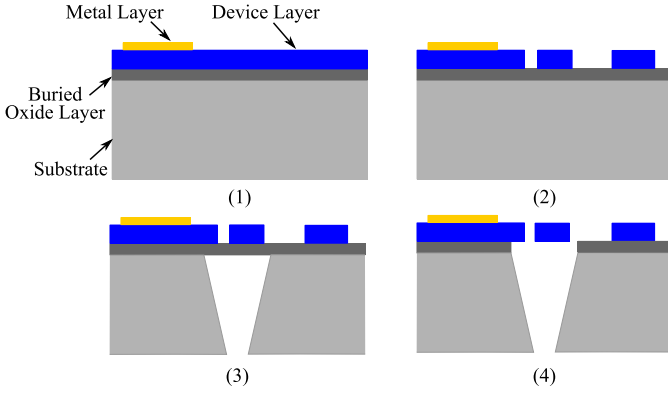
Fig. 2. The fabrication steps of the SOIMUMPs fabrication process. 1) Deposition and patterning of the metal layer. 2) Patterning of the device layer using DRIE. 3) Patterning the substrate using RIE and DRIE. 4) Releasing of the device by etching the buried oxide layer.

AFM imaging. Other aspects of the device's design such as the piezoresistive sensor in the Y direction are also illustrated in the close-up views.

As seen in Fig. 3, two pairs of dummy resistors are implemented separately on the chip. These resistors are tilted beams with the same dimensions as the piezoresistive sensors without gold coating. They do not experience mechanical stress during the nanopositioner operation. However, their electrothermal conditions are nearly identical to those of piezoresistors. Hence, these dummy resistors can be used in a properly designed readout circuit to alleviate parasitic effects such as ambient temperature variations at the sensors' output.

A. Folded-Beam Spring

A schematic of a folded-beam spring with three beams is depicted in Fig. 4a. The in-plane stiffness of the folded spring is obtained by calculating the displacement of the shuttle beam under the influence of a known external force denoted by F_{ext}. Three separate Cartesian coordinate systems are defined for the beams, and their deflection functions are designated by y_i ($i = 1$ to 3). The free body diagrams of the beams are also shown in Fig. 4b. Based on the beams' loading condition, (1), (2), and (3) are written for their deflection functions using the Euler-Bernoulli theory:

$$y_1(x_1) = \frac{M_0}{2EI_1}x_1^2 - \frac{F_{ext}}{6EI_1}x_1^3 + C_1x_1 + C_2 \qquad (1)$$

$$y_2(x_2) = \frac{F_{ext}}{6EI_2}x_2^3 - \frac{M_2}{2EI_2}x_2^2 + C_3x_2 + C_4 \qquad (2)$$

$$y_3(x_3) = \frac{M_3}{2EI_3}x_3^2 - \frac{F_{ext}}{6EI_3}x_3^3 + C_5x_3 + C_6 \qquad (3)$$

where I_i ($i = 1$ to 3) are the second moment of the beams' cross-sectional area. For in-plane bending, these moments can be obtained as:

$$I_i = \frac{tb_i^3}{12} \qquad (4)$$

where b_i is the width of each beam and t denotes their thickness (the out-of-plane dimension). The unknowns in the deflection functions can be determined using mechanical

boundary conditions. For the first beam at its anchor point we have:

$$y_1(x_1) = y_1'(x_1) = 0 \ at \ x_1 = 0. \qquad (5)$$

Ignoring the length of the connecting segments, (6) is written for the point (A) where the first and second beams are connected.

$$\begin{cases} y_1(x_1 = l_1) = y_2(x_2 = l_2) \\ y_1'(x_1 = l_1) = y_2'(x_2 = l_2) \end{cases} \qquad (6)$$

Similarly for the second and third beams, (7) is valid.

$$\begin{cases} y_2(x_2 = 0) = y_3(x_3 = 0) \\ y_2'(x_2 = 0) = y_3'(x_3 = 0) \\ y_3'(x_3 = l_3) = 0 \end{cases} \qquad (7)$$

Finally, two extra boundary conditions are written based on the static equilibrium of the structure as:

$$\begin{cases} M_2 = M_0 + F_{ext}(l_2 - l_1) \\ M_0 = M_3 + F_{ext}(l_3 + l_1 - l_2). \end{cases} \qquad (8)$$

The deflection profiles can be obtained by substituting the deflection functions into the boundary-conditions and solving the resulting linear system of equations. The displacement of the shuttle beam (d) and the in-plane stiffness of the folded spring (K) are then calculated as:

$$d = y_3(x_3 = l_3) \implies K = F_{ext}/d. \qquad (9)$$

Using this analytical analysis, the dimensional tuning of the folded spring is possible during the design. Note that due to the similar boundary conditions, the same analytical approach can be used to obtain the out-of-plane stiffness. In this case, the second moment of the beams' cross-sectional area should be re-calculated for the out-of-plane bending condition as:

$$I_{iz} = \frac{t^3 b_i}{12}. \qquad (10)$$

B. Discussion on the Design

A larger out-of-plane stiffness (compared to the in-plane stiffness) can enhance the nanopositioner's performance. This will potentially improve the stability of the nanopositioner during in-plane scans, specifically while an AFM probe is also landed on the stage. In addition, by properly tuning the in-plane and out-of-plane stiffnesses, the fundamental resonant mode of the system will be in-plane. Thus, this mode becomes fully observable by the displacement sensors, which makes the control problem less challenging.

The in-plane and out-of-plane stiffnesses of the folded springs cannot be changed independently by dimensional tuning only. This is due to the constant thickness of the entire structure. However, using (4) and (10), this issue can be tackled by decreasing the beams' width (b_i) while increasing their number proportionally. In this approach, the in-plane stiffness of the folded springs can be decreased while their out-of-plane stiffness remains almost unchanged. As shown in Fig. 3, we have implemented this method by
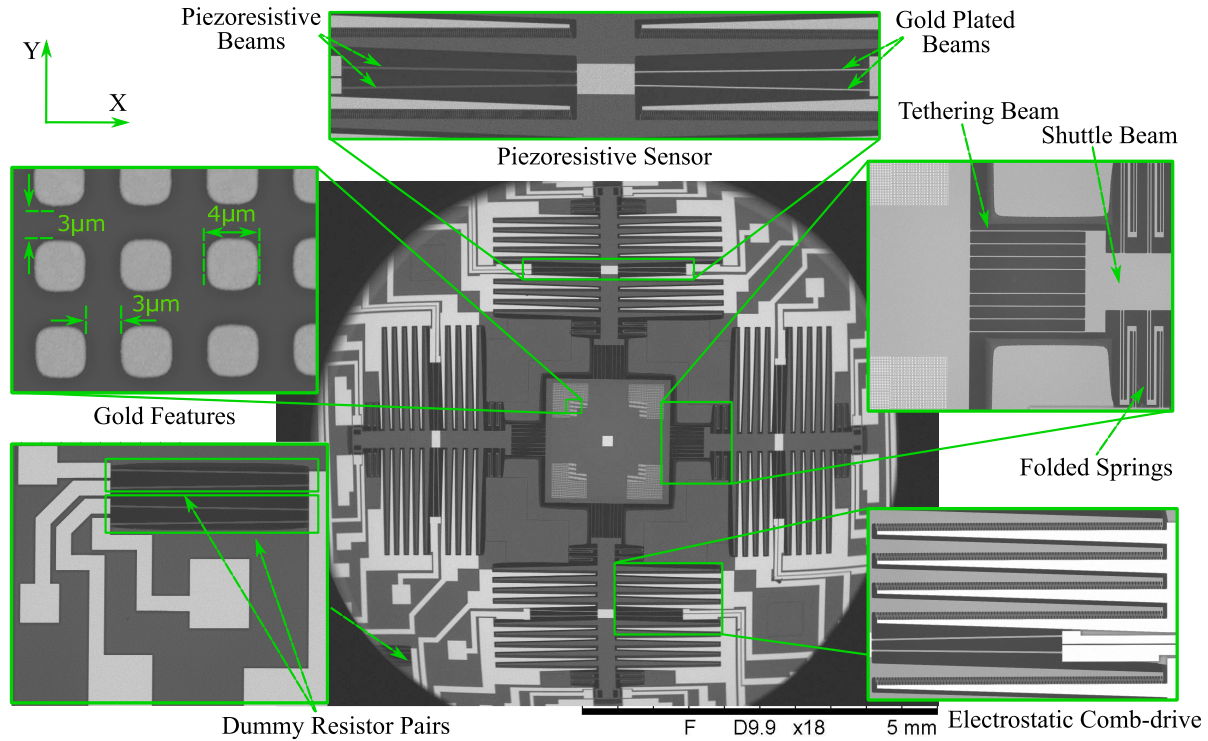
Fig. 3. SEM image of the MEMS nanopositioner. The close-up views show the folded beam springs, the tethering beams, and the piezoresistive sensors. The close-up view on the bottom-left shows two pairs of on-chip dummy resistors.
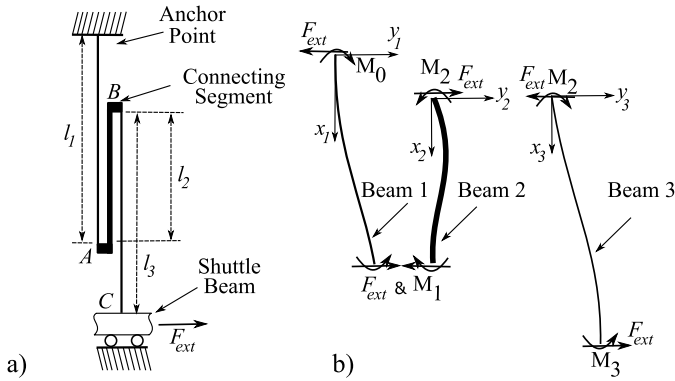

Fig. 4. a) Schematic of a folded beam spring. b) Free body diagrams of each beam, ignoring the dimensions of the small connecting segments.

TABLE I

GEOMETRICAL AND MATERIAL PROPERTIES
OF THE PROPOSED MEMS NANOPOSITIONER

Young modulus $E = 169\,$GPa		Thickness: $25\,\mu$m
Tilted beams	Normal Length $h = 1$mm	Width $w = 10\,\mu$m
	Inclination distance, angle: $\Delta = 15\,\mu$m, $\delta = 0.86°$	
Comb finger	Air gap: $2\,\mu$m	Engagement:$12\,\mu$m
	Length: $26\,\mu$m	Width:$2\,\mu$m
Comb structures	Trapezoidal: Length:1536μm, Bases: 20, $75\,\mu$m	
Shuttle beams	$2353\,\mu$m $\times$ $250\,\mu$m	
Tethering beams	$500\,\mu$m $\times$ $5\,\mu$m, 8 on each side	
Folded springs	Beam 1: Length: $334\,\mu$m, width:$4.5\,\mu$m	
	Beam 2: Length: $300\,\mu$m, Width:$12\,\mu$m	
	Beam 3: Length: $391\,\mu$m, Width:$5\,\mu$m	
	Connecting segment: $13\,\mu$m	

replacing "Beam 1" and "Beam 3" with two beams with more slenderness resulting in the folded springs with 5 beams.

The dimensional tuning is performed analytically and by using a finite element model (FEM) which is constructed in CoventorWare software. The material properties and the tuned dimensions of the nanopositioner are summarized in Table I. In Fig. 5, the first and second vibration mode shapes of the device are also presented. The first in-plane resonant modes is obtained at 4274 Hz for each axis. The first out-of-plane frequency is located at 6965 Hz, which is 63 % larger than the fundamental in-plane resonance modes. The out-of-plane stiffness of the stage is obtained through FEM as 408 N/m. Since the AFM contact-mode cantilevers typically have an out-of-plane stiffness below 10 N/m [31] and operate at a force

set-point in the range of tens of nano-Newtons, the stage is expected to have a negligible out-of-plane deflection during contact-mode imaging.

The force-displacement characteristic of the folded springs is also expected to be more linear compared with the typical clamped-guided beams. The lateral stiffness of each folded spring in this design is 8.47 N/m obtained using the analytical model. The folded springs may be replaced by straight clamped-guided beams with the width of 5.36 μm and with the same stiffness. This width is calculated assuming a length of $(l_1 + l_3 - l_2)$ and using the equation for lateral stiffness of clamped-guided beams in [32]. As also discussed in [33], it can be shown that the force-displacement behavior of the clamped-guided Euler-Bernoulli beams deviates from linear more
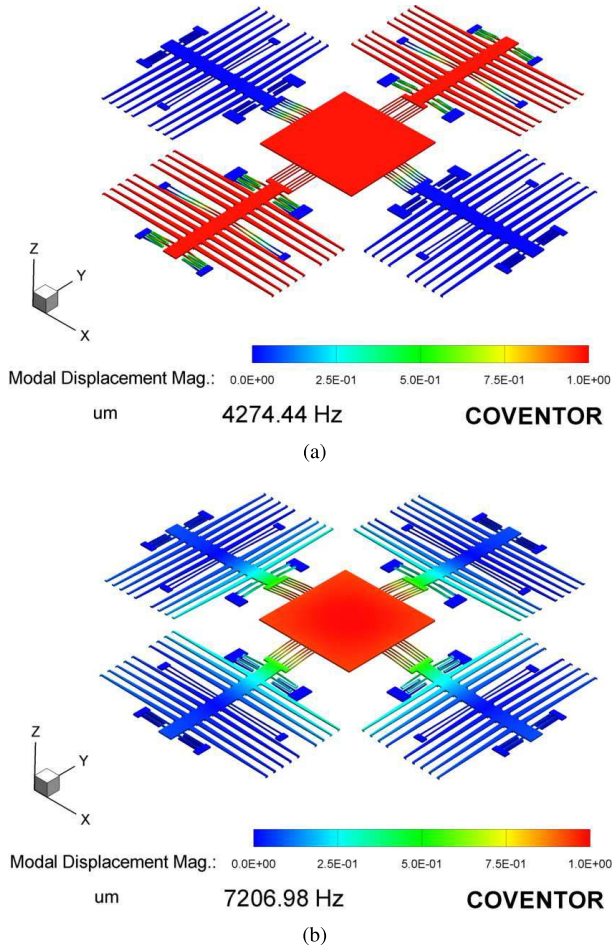
(a)

(b)

Fig. 5.   The FEM results obtained for the device. The first in-plane and out-of-plane modes are depicted in (a) and (b), respectively.

Fig. 6.   The force-displacement characteristics of eight folded beams obtained by FEM in the linear and nonlinear conditions.

(a)

(b)

Fig. 7.   (a) Schematic of the sensing mechanism for the X axis. The same mechanism is symmetrically implemented in the Y direction. (b) Schematic of the actuation circuit for each axis.

than 10% as their guided-end displacement exceeds 43% of their width; in this case this is about 2.3 μm of displacement. This nonlinearity mainly arises due to the development of the axial tensile force while the beam's guided end moves [33]. In the folded spring, however, the transverse displacement will be divided between the beams, reducing the axial force along each of them. Thus, more linear behavior is expected.

The linearity of the folded springs is examined using FEM. In the model, eight folded springs with the dimensions reported in Table I are attached to a shuttle beam with the same configuration depicted in Fig. 1. Simulations are performed by applying different forces to the shuttle beam and obtaining the displacement under both linear and nonlinear conditions. In the linear simulation, the software calculates the flexibility matrix (the inversion of the stiffness matrix) of the structure only once. In the nonlinear approach, the software divides a loading condition by a number of smaller increments, and instead of using an initial flexibility matrix, it constructs a stiffness matrix and inverts it in each increment.

The displacements of the shuttle beam are presented in Fig. 6 for both analytical and finite element models. The analytical model and the linear FEM show linear trends with about 6% difference in their slope. This is most likely due to ignoring of the connecting segments' length in the
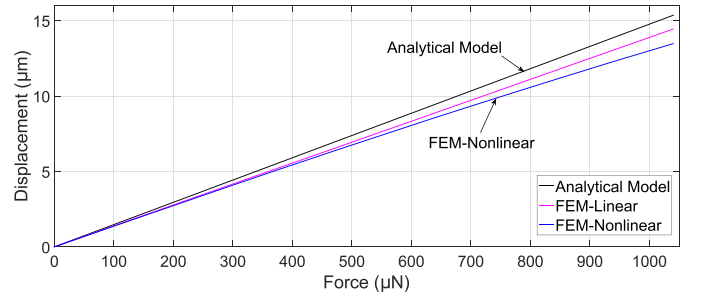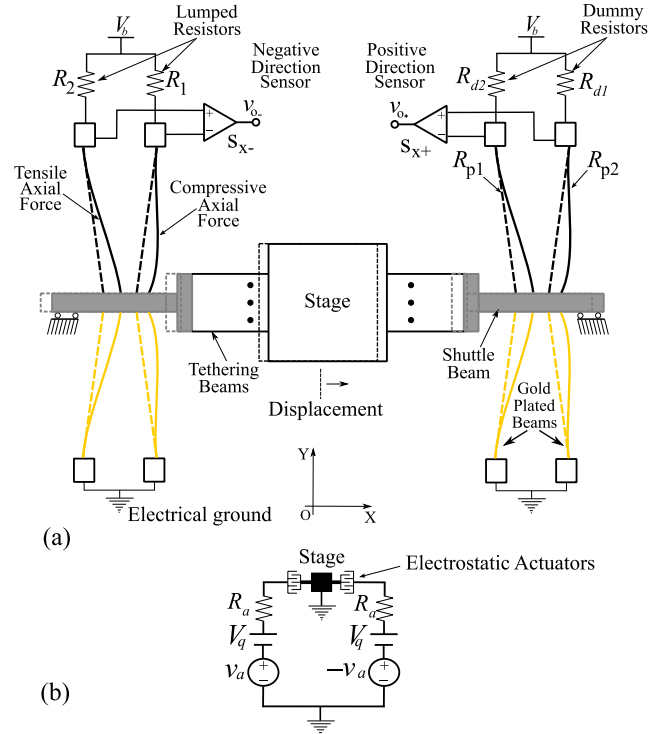
analytical model. A hardening behavior is observable from the results obtained by the nonlinear FEM. Comparing the linear and nonlinear FEM, for a given force, the deviation from the linear is below 4% until more than 10 μm of shuttle beam displacement. Hence, a more linear performance is expected from the folded springs rather than clamped-guided beams.

III. PIEZORESISTIVE SENSOR

The working principle of the bulk piezoresistive sensors and their structural configuration in the X axis are schematically illustrated in Fig. 7. Along the Y axis, the same configuration is employed. The movement of the stage along the X axis induces in-plane deflections in the beams. However, due to the slightly tilted geometry, one beam in each pair experiences a tensile axial force while the force along the other beam is compressive. Since the beams feature almost identical

doping conditions, these longitudinal forces lead to opposite variations in their electrical resistances (R_{p1} and R_{p2}) mainly due to the piezoresistivity of the silicon. The gold-plated beams with a negligible resistance are electrically grounded. The resistance variations of R_{p1} and R_{p2} are subsequently converted to output voltages using a Wheatstone bridge in a half bridge configuration. Finally, the voltages are differentially amplified by an instrumentation amplifier (In-amp) at the sensor output. We previously demonstrated that the output voltage of this sensing configuration is proportional to the displacement of the shuttle beam [28], [29].

As shown in Fig. 7a, two piezoresistive sensors are implemented for the X axis designated by $Sx+$ for the positive and $Sx-$ for the negative side. Similarly in the Y axis, $Sy+$ and $Sy-$ denote the sensor in the positive and negative directions, respectively. To further investigate the feedthrough behavior of the sensors, both dummy and lumped resistors are used to complete their readout circuitry as shown in Fig. 7a. The dummy resistors are used in the Wheatstone bridge for $Sx+$ and $Sy-$, while the lumped resistors are used for $Sx-$ and $Sy+$. All these sensors are characterized as presented next.

IV. CHARACTERIZATION

Having comb structures on both sides of each axis allows us to implement a linear actuation mechanism [6]. The actuation circuit is schematically shown in Fig. 7b. Two actuation voltages designated by v_a with opposite signs superimposed on a constant dc voltage ($V_q = 45$ V) are applied to the stationary comb-drives. The stage and the moving combs are electrically grounded via the gold-plated tilted beams. In this method, the net actuating force experienced by the stage is a linear function of ($V_q \times v_a$). This can significantly mitigate the problem of quadratic relationship in electrostatic actuators [6].

The bias voltage for all sensors (V_b in Fig. 7a) is adjusted to 6 V. In the absence of the actuation voltage, when the stage is at the equilibrium position, the outputs of the sensors are adjusted to zero using potentiometers in their readout circuits.

A. Static Response

The stage displacement is experimentally measured in the X and Y axes using a Polytec MSA-050-3D Micro System Analyzer (MSA). Fig. 8a plots the displacement of the stage as a function of the actuation voltage (v_a). A linear actuation-displacement relationship is observed, where maximum displacements of $\pm 8 \, \mu$m and $\pm 7.5 \, \mu$m are obtained in the X and Y directions, respectively.

During the static test, the outputs of all piezoresistive sensors are also recorded simultaneously and are plotted against the stage displacement in Fig. 8b. A linear relationship between the sensor outputs and the stage displacement is clear for all sensors. Using Fig 8b, the calibration factors of the sensors, defined as the sensor output in 1 μm stage displacement, are obtained and reported in Table II.

The cross coupling between the X and Y axes is the other feature investigated. An experiment is performed by applying a large sinusoidal displacement (about 14 μm peak-to-peak)
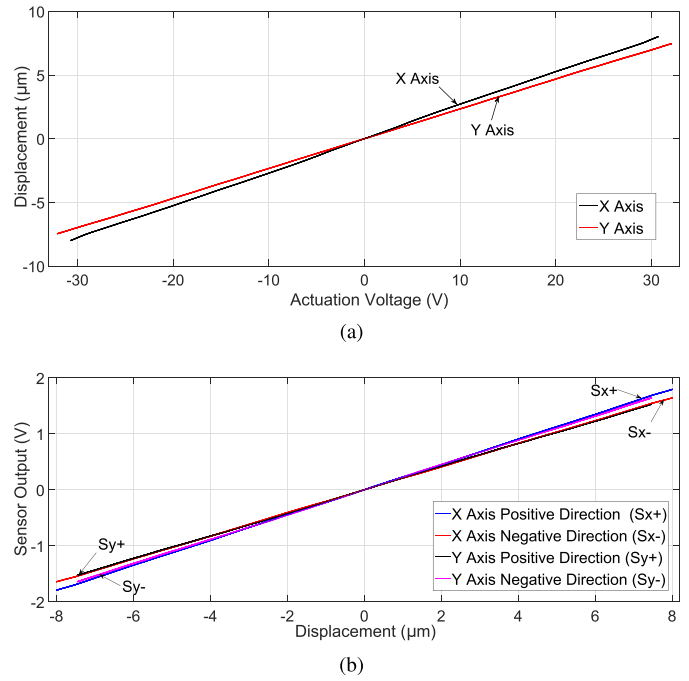

Fig. 8. (a) The displacement of the stage in both axes versus actuation voltage (v_a) obtained by the MSA. (b) The outputs of piezoresistive sensors versus the stage displacement for both axes.

TABLE II
CALIBRATION FACTORS AND THE RESOLUTION
OF THE PIEZORESISTIVE SENSORS

Characteristics	X axis		Y axis	
	$Sx+$	$Sx-$	$Sy+$	$Sy-$
Calibration factor (V/μm)	0.227	0.208	0.219	0.236
Resolution (nm)	2	1.8	1.8	1.9

to one axis while the sensors' outputs on the other axis are recorded. The obtained results indicate a negligible cross coupling of about -39.6 dB between the two axes.

B. Noise and Resolution

The sensors' noise is recorded in the time domain, sampled at 128 kHz over a time duration of 25 s. The resolution of the sensors is defined as the root mean square (rms) value of the noise signal converted to displacement using the calibration factors. As reported in Table II, a resolution below 2 nm is obtained for all sensors.

C. Dynamic Response

The frequency response is measured by exciting the nanopositioner using a chirp signal with a bandwidth of 100 kHz as v_a. The displacement of the stage is recorded using the MSA and the piezoresistive sensors, and the resulting frequency responses of the device for both axes are shown in Fig. 9. The first in-plane resonances occur at 3626 Hz and 3944 Hz for the X and Y axes, respectively. The second in-plane translational mode is observed at about 50 kHz for both axes.
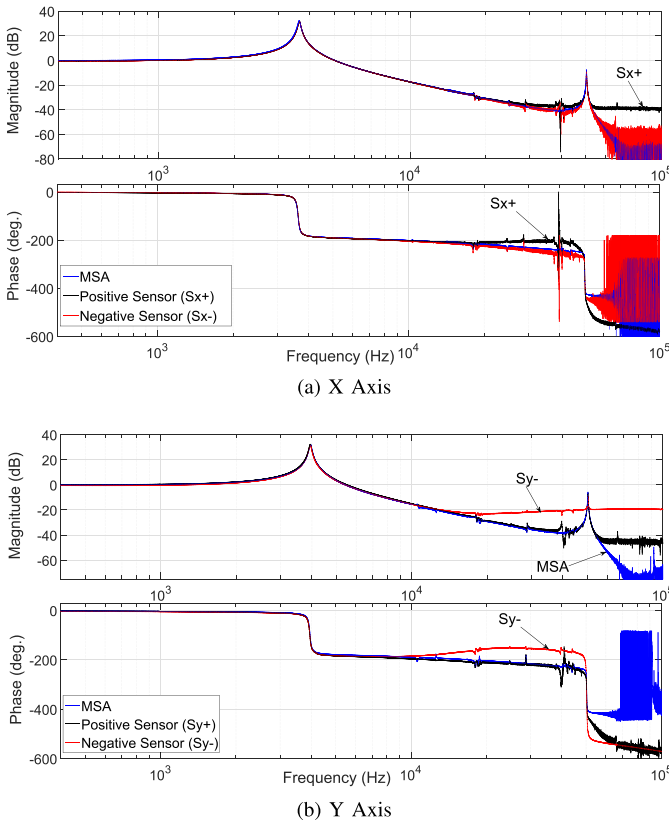
(a) X Axis

(b) Y Axis

Fig. 9. The frequency response of the MEMS nanopositioner in the X (a) and Y (b) directions obtained using the MSA, and the piezoresistive sensors on either sides. A feedthrough signal is mostly observable at high frequencies in the response of $Sx+$ and $Sy-$.

(a) X axis

(b) Y axis

Fig. 10. The sensing and feedthrough signals are compared for all sensors for the X (a) and Y (b) axes.

A high-pass behavior, however, is observable in both axes sensor outputs. This is due to the feedthrough signal from actuation [29]. The presence of this signal leads to a reduction in the measurement bandwidth of the sensor. As seen in Fig. 9, this signal predominantly reduces the effective bandwidth of the $Sx+$ and $Sy-$ to about 30 kHz and 20 kHz, respectively.

Although the feedthrough signal reduces the effective bandwidth of these sensors, they adequately capture dynamics of the device without inducing notable phase delay up to at least 20 kHz. This bandwidth is still more than five times greater than the first in-plane resonant mode of the nanopositioner (at about 4 kHz), and is sufficient for the implementation of a feedback controller to damp this resonant mode. In addition, $Sx-$ and $Sy+$ demonstrate more than 55 kHz of sensing bandwidth, which is more than ten times higher than the first mechanical resonant frequency. These sensors also capture the second translational resonant mode of the stage. Hence, they can potentially be used to implement a feedback controller for this mode, if needed. Note that the achieved bandwidths are greater than the typical 5 kHz to 10 kHz expected bandwidth of on-chip electrothermal sensors [6], [19], [34], [35].

V. THE FEEDTHROUGH

The feedthrough phenomenon is further investigated by recording all sensor outputs while the dc bias of the actuation circuit is switched off (i.e. $V_q = 0$). The net actuation force is
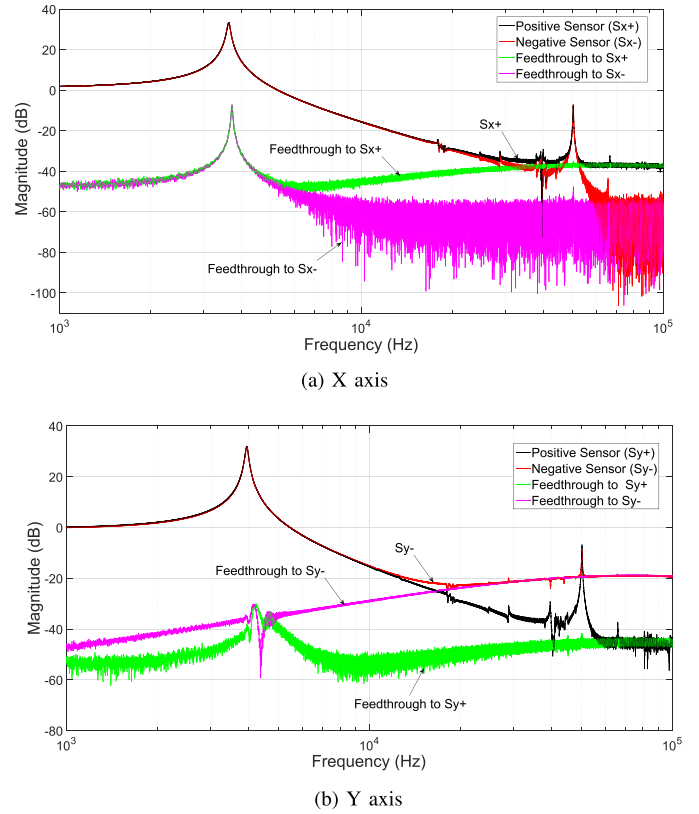
a function of $V_q \times v_a$ [32]. Therefore, the stage experiences a negligible force and remains stationary. Consequently, the feedthrough signal from actuation (v_a) will be dominant at the sensors' output.

In Fig. 10, the feedthrough measurements for all sensors are plotted against their frequency responses. Let us define the corner frequency as a frequency at which the feedthrough signal attains the same magnitude as the main sensor signal originating from the stage displacement. Clearly, the corner frequency has a direct effect on the bandwidth of the sensors. In the X direction, $Sx-$ shows a negligible feedthrough in the 100 kHz frequency range with no visible corner frequency, while $Sx+$ has a corner frequency of approximately 55 kHz, limiting the bandwidth of this sensor. In the Y axis, $Sy+$ demonstrates a corner frequency of about 60 kHz, while a corner frequency of about 25 kHz for $Sy-$ leads to its significantly narrower bandwidth.

The piezoresistive sensors have identical dimensions as those reported in [28]. However, they demonstrate a significantly larger bandwidth. The bandwidth improvement is the result of modifications made to the configuration of the piezoresistive sensors and the on-chip routing of the sensing and actuation tracks. As we analytically discussed in [29], the feedthrough signal is believed to exist due to the presence of parasitic electrical elements between on-chip sensing and actuation tracks. In this design, the tilted beams of each sensor are placed beside each other and connected to the shuttle beam 40 μm apart. This is on the contrary of the design in [29]
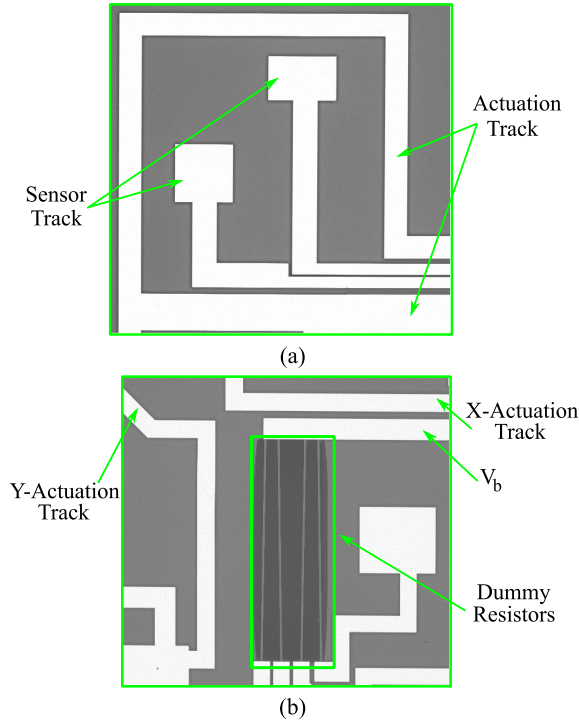
(a)

(b)

Fig. 11.   (a) SEM image of the sensing and actuating tracks on one side of the device. (b) The dummy resistors' position relative to the actuation tracks.
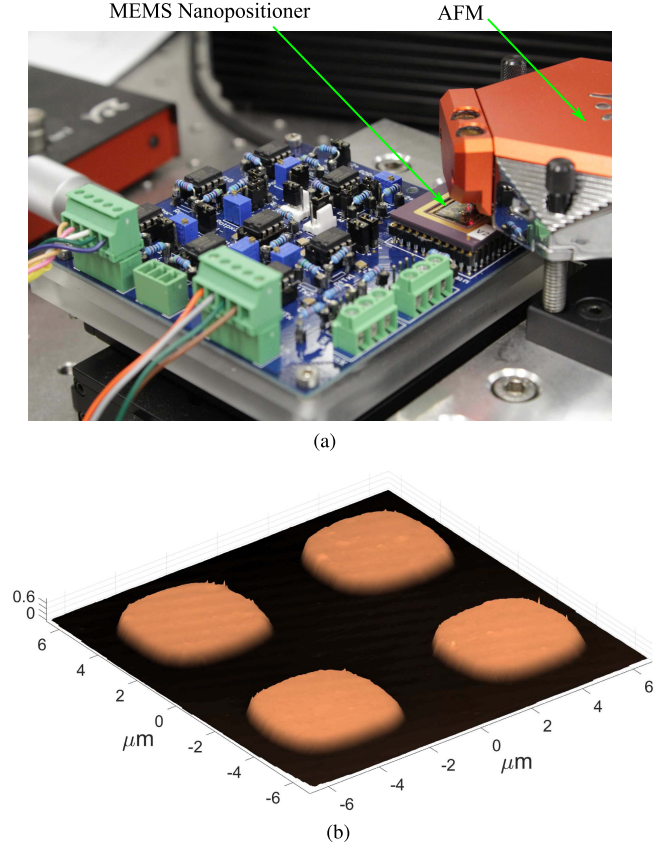

(a)

(b)

Fig. 12.   (a) The test setup for AFM imaging. The packaged MEMS nanopositioner is mounted on a PCB with actuation and sensing circuits. (b) The AFM image of the gold features with the height of about 520 nm.

where the tilted beams are located on the opposite sides of the stage. Having tilted beams near each other enables us to route the sensor signals close to one another and enclose them with the high-voltage actuation signal track on each side of the device. Fig. 11a illustrates a SEM image of these tracks. Here, parasitic elements between each sensing track and the actuation path are expected to be almost identical, leading to the induction of an approximately equal feedthrough signal on each sensing track. The differential structure of the readout circuit shown in Fig. 7a as well as the in-amp's common mode rejection characteristic then cancel these two signals. As further discussed in the Appendix, this configuration was not used in [28], leading to an inferior sensor bandwidth.

Although all sensors in this nanopositioner generally show improvements in their frequency domain responses, they demonstrate different bandwidths. This can be explained based on whether the on-chip dummy resistors or external lumped resistors are utilized in the sensors' readout circuitry. $Sx+$ and $Sy-$, with relatively narrower bandwidths, have on-chip dummy resistors in their readout circuits, whereas lumped resistors are used for $Sx-$ and $Sy+$. As shown in Fig. 11b, the actuation signal tracks are routed adjacent to the on-chip dummy resistors due to the limited space on the MEMS die. The additional parasitic elements originating from this configuration exacerbate the cross-talk between the actuation and the sensing signals. Note that the excessive parasitic elements at the in-amp input can potentially reduce its effective common mode rejection ratio and, as a result, increase the feedthrough signal at the sensors' output.

The bandwidth enhancement indicates that a proper arrangement of sensing and high-voltage actuation tracks

relative to each other will have a significant effect on the feedthrough signal level. Further improvement in the bandwidth of $Sx+$ and $Sy-$ is expected by implementing the dummy resistors away from the actuation tracks or enclosing them within one actuation path.

VI. AFM Imaging

The proposed nanopositioner is used as the scanning stage under a commercial Nanosurf Easyscan2 AFM. The test setup is illustrated in Fig. 12a, where the packaged MEMS nanopositioner is mounted on a custom-designed PCB. The nanopositioner is operated in open loop and the imaging is performed via constant-height contact mode. The gold features on the stage are used as the reference pattern. Before imaging, the AFM probe is landed on the stage with a force set-point of 15 nN. Then, the embedded probe nanopositioner of the Nanosurf AFM is bypassed. The scan is performed in a $12 \mu m \times 12 \mu m$ window size using the raster scan method. During the scan, a triangular signal with 10 Hz frequency is applied to the X axis, and the Y axis follows a slow ramp. In Fig. 12b, the obtained image of the gold features is shown. The tip deflection of the probe is measured using the AFM's optical sensor. The topography of the features is obtained by plotting their optically measured heights against position measurements obtained from the piezoresistive sensors. The sampling rate of the data acquisition system is adjusted to achieve an image with 400×400 pixels.
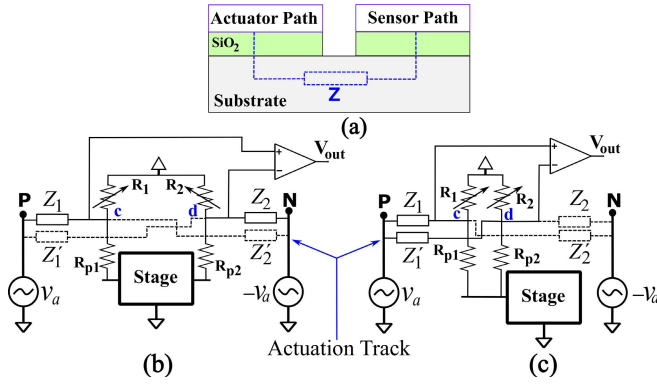
Fig. 13. (a) Parasitic impedance between actuation and sensing tracks. Small signal model of the readout circuit of the piezoresistive sensor: (b) in [29], and (c) in one side of the 2DOF MEMS nanopositioner.

VII. CONCLUSION

A 2DOF MEMS nanopositioner is proposed and used as a scan table within an AFM. The bulk piezoresistivity of tilted clamped-guided beams is exploited for on-chip displacement sensing. Better than 20 kHz of sensing bandwidths are experimentally demonstrated by modifying the sensors design. Folded springs implemented as part of the nanopositioners suspension and their mechanical characteristics are investigated using analytical and finite element models. Characterization of the nanopositioner demonstrates a displacement range and an in-plane resonance mode of above 15 μm and 3.6 kHz, respectively in both axes. The high sensing bandwidth plus the nanopositioner's linear behavior and its high out-of-plane stiffness make this device a promising platform for various nanopositioning applications such as in on-chip AFMs.

VIII. FUTURE WORK

Further bandwidth improvement in the piezoresistive sensors is possible by implementing a feedthrough cancellation technique [36]. Future work will involve the implementation of high-speed controllers on the device. The frequency response of the nanopositioner makes it possible to implement high-performance control systems. The controlled nanopositioner can then be used as a scanner stage within an AFM to realize on-chip video rate imaging.

APPENDIX

Here, the underlying reasons for the improvement in the bandwidth of the piezoresistive sensors in comparison with those reported in [29] are further discussed. Fig. 13a schematically shows the actuation and sensing tracks, which are traced on a low-doped silicon substrate [30]. These tracks are electrically insulated via a 2 μm-thick oxide layer. The electrical characteristics of the oxide layer and the substrate are modeled as a parasitic impedance designated by $Z(j\omega)$ [29]. The dimension of the tracks and their spatial configuration affect the parasitic impedance. Technically, the impedance between the tracks routed far away from each other are expected to be larger than adjacent tracks of the same dimension.

The small signal model of the readout circuit for the sensor implemented in a 1 DOF nanopositioner in [29] and the device in this work are respectively shown in Figs. 13b and c. The parasitic impedances (indicated with dashed lines) are expected to be larger than those with the solid lines. The linear actuation mechanism was also implemented for the nanopositioner in [29]. The induced cross-talk voltages on the points c and d from the actuation signals (v_a and $-v_a$) respectively are:

$$v_c(j\omega) = \frac{R_{eq1}}{Z_1(j\omega) + R_{eq1}} v_a \qquad (11)$$

$$v_d(j\omega) = -\frac{R_{eq2}}{Z_2(j\omega) + R_{eq2}} v_a \qquad (12)$$

where $R_{eq1} = R_{P1}||R_1$ and $R_{eq2} = R_{P2}||R_2$. A_{in} is assumed to be the gain of the instrumentation amplifiers, thus the cross-talk voltage at the sensor output is:

$$v_{out} = A_{in} \left(\frac{R_{eq1}}{Z_1(j\omega) + R_{eq1}} + \frac{R_{eq2}}{Z_2(j\omega) + R_{eq2}} \right) v_a. \qquad (13)$$

As is visible in (13), the amplified feedthrough signals from the actuation tracks N and P will appear at the sensor output. Note that the effect of $Z'_{1,2}(j\omega)$ is ignored as they are larger than $Z_{1,2}(j\omega)$. This model is further discussed and validated with experimental data in [29].

In the improved design, however, the tilted beams are placed on one side of the stage and the sensing signal routing are changed. Hence, as visible in Fig. 13c, the impedance $Z_1(j\omega)$ and $Z'_1(j\omega)$ are smaller than $Z_2(j\omega)$ and $Z'_2(j\omega)$, so the actuation cross-talk through them will be larger than the parasitic impedance from the other side of the stage. In addition, as the sensing tracks are routed close to each other and are enclosed by the actuation P, the $Z_1(j\omega)$ and $Z'_1(j\omega)$ are expected to be almost equal. The output of the sensor due to the cross-talk form P is:

$$v_{out} = A_{in} \left(\frac{R_{eq1}}{Z_1(j\omega) + R_{eq1}} - \frac{R_{eq2}}{Z'_1(j\omega) + R_{eq2}} \right) v_a. \qquad (14)$$

If the device is symmetrically fabricated, the cross-talk will be ideally zero at the output. Equation (14) is valid for the feedthrough signal from the other side of the stage (i.e. N) provided that $Z_1(j\omega)$ and $Z'_1(j\omega)$ are replaced by $Z_2(j\omega)$ and $Z'_2(j\omega)$. This cross-talk will be smaller in magnitude, and, as $Z_2(j\omega) \approx Z'_2(j\omega)$ due to the sensing tracks routing, it will be canceled out significantly at the output.

REFERENCES

[1] K. Salaita, Y. Wang, and C. A. Mirkin, "Applications of dip-pen nanolithography," *Nature Nanotechnol.*, vol. 2, no. 3, pp. 145–155, Mar. 2007.

[2] L. Zhang and J. Dong, "High-rate tunable ultrasonic force regulated nanomachining lithography with an atomic force microscope," *Nanotechnology*, vol. 23, no. 8, pp. 085303-1–085303-9, Feb. 2012.

[3] Y. K. Yong, S. O. Reza Moheimani, B. J. Kenton, and K. K. Leang, "Invited review article: High-speed flexure-guided nanopositioning: Mechanical design and control issues," *Rev. Sci. Instrum.*, vol. 83, no. 12, p. 121101, Dec. 2012.

[4] E. Eleftheriou, "Nanopositioning for storage applications," *Annu. Rev. Control*, vol. 36, no. 2, pp. 244–254, Dec. 2012.

[5] A. Pantazi *et al.*, "Control of MEMS-based scanning-probe data-storage devices," *IEEE Trans. Control Syst. Technol.*, vol. 15, no. 5, pp. 824–841, Sep. 2007.

[6] M. Maroufi, A. Bazaei, and S. O. Reza Moheimani, "A high-bandwidth MEMS nanopositioner for on-chip AFM: Design, characterization, and control," *IEEE Trans. Control Syst. Technol.*, vol. 23, no. 2, pp. 504–512, Mar. 2014.

[7] S. Yoo, J.-Y. Jin, J.-G. Ha, C.-H. Ji, and Y.-K. Kim, "Two-dimensional optical scanner with monolithically integrated glass microlens," *J. Micromech. Microeng.*, vol. 24, no. 5, p. 055009, 2014.

[8] O. Solgaard, A. A. Godil, R. T. Howe, L. P. Lee, Y.-A. Peter, and H. Zappe, "Optical MEMS: From micromirrors to complex systems," *J. Microelectromech. Syst.*, vol. 23, no. 3, pp. 517–538, Jun. 2014.

[9] X. Liu, K. Kim, and Y. Sun, "A MEMS stage for 3-axis nanopositioning," *J. Micromech. Microeng.*, vol. 17, no. 9, p. 1796, 2007.

[10] Y.-S. Kim, J.-M. Yoo, S. H. Yang, Y.-M. Choi, N. G. Dagalakis, and S. K. Gupta, "Design, fabrication and testing of a serial kinematic MEMS *XY* stage for multifinger manipulation," *J. Micromech. Microeng.*, vol. 22, no. 8, p. 085029, 2012.

[11] M. Olfatnia, L. Cui, P. Chopra, and S. Awtar, "Large range dual-axis micro-stage driven by electrostatic comb-drive actuators," *J. Micromech. Microeng.*, vol. 23, no. 10, p. 105008, 2013.

[12] J. Dong and P. M. Ferreira, "Electrostatically actuated cantilever with SOI-MEMS parallel kinematic *XY* stage," *J. Microelectromech. Syst.*, vol. 18, no. 3, pp. 641–651, Jun. 2009.

[13] J.-I. Lee, X. Huang, and P. Chu, "Nanoprecision MEMS capacitive sensor for linear and rotational positioning," *J. Microelectromech. Syst.*, vol. 18, no. 3, pp. 660–670, Jun. 2009.

[14] B. Koo, X. Zhang, J. Dong, S. M. Salapaka, and P. M. Ferreira, "A 2 degree-of-freedom SOI-MEMS translation stage with closed-loop positioning," *J. Microelectromech. Syst.*, vol. 21, no. 1, pp. 13–22, Feb. 2012.

[15] L. Ji, Y. Zhu, S. O. Reza Moheimani, and M. R. Yuce, "A micromachined 2DOF nanopositioner with integrated capacitive displacement sensor," in *Proc. IEEE Sensors*, Nov. 2010, pp. 1464–1467.

[16] L. L. Chu and Y. B. Gianchandani, "A micromachined 2D positioner with electrothermal actuation and sub-nanometer capacitive sensing," *J. Micromech. Microeng.*, vol. 13, no. 2, p. 279, Jan. 2003.

[17] J. Dong and P. M. Ferreira, "Simultaneous actuation and displacement sensing for electrostatic drives," *J. Micromech. Microeng.*, vol. 18, no. 3, p. 035011, 2008.

[18] C. K. Pang *et al.*, "Design, fabrication, sensor fusion, and control of a micro *X–Y* stage media platform for probe-based storage systems," *Mechatronics*, vol. 19, no. 7, pp. 1158–1168, Oct. 2009.

[19] M. A. Lantz, G. K. Binnig, M. Despont, and U. Drechsler, "A micromechanical thermal displacement sensor with nanometre resolution," *Nanotechnology*, vol. 16, no. 8, pp. 1089–1094, 2005.

[20] Y. Zhu, A. Bazaei, S. O. Reza Moheimani, and M. R. Yuce, "Design, modeling, and control of a micromachined nanopositioner with integrated electrothermal actuation and sensing," *J. Microelectromech. Syst.*, vol. 20, no. 3, pp. 711–719, Jun. 2011.

[21] B. Krijnen *et al.*, "A single-mask thermal displacement sensor in MEMS," *J. Micromech. Microeng.*, vol. 21, no. 7, p. 074007, 2011.

[22] M. Maroufi, A. G. Fowler, A. Bazaei, and S. O. Reza Moheimani, "High-stroke silicon-on-insulator MEMS nanopositioner: Control design for non-raster scan atomic force microscopy," *Rev. Sci. Instrum.*, vol. 86, pp. 023705-1–023705-12, 2015.

[23] E. Guliyev *et al.*, "Quasi-monolithic integration of silicon-MEMS with piezoelectric actuators for high-speed non-contact atomic force microscopy," *Meas. Sci. Technol.*, vol. 23, no. 7, pp. 074012-1–074012-8, 2012.

[24] Y.-S. Choi, Y. Zhang, and D.-W. Lee, "A thermal-driven silicon micro *xy*-stage integrated with piezoresistive sensors for nano-positioning," *J. Micromech. Microeng.*, vol. 22, no. 5, p. 074012, 2012.

[25] A. A. Barlian, W.-T. Park, J. R. Mallon, A. J. Rastegar, and B. L. Pruitt, "Review: Semiconductor piezoresistance for microsystems," *Proc. IEEE*, vol. 97, no. 3, pp. 513–552, Mar. 2009.

[26] O. Hansen and A. Boisen, "Noise in piezoresistive atomic force microscopy," *Nanotechnology*, vol. 10, no. 1, p. 51, 1999.

[27] X. Wei and A. A. Seshia, "Differential piezoresistive sensing in a bulk-mode micromechanical resonator," *IET Micro Nano Lett.*, vol. 8, no. 2, pp. 107–110, Feb. 2013.

[28] A. Bazaei, M. Maroufi, A. Mohammadi, and S. O. Reza Moheimani, "Displacement sensing with silicon flexures in MEMS nanopositioners," *J. Microelectromech. Syst.*, vol. 23, no. 3, pp. 502–504, Jun. 2014.

[29] M. Maroufi, A. Bazaei, A. Mohammadi, and S. O. Reza Moheimani, "Tilted beam piezoresistive displacement sensor: Design, modeling, and characterization," *J. Microelectromech. Syst.*, vol. 24, no. 5, pp. 1594–1605, Oct. 2015.

[30] A. Cowen, G. Hames, D. Monk, S. Wilcenski, and B. Hardy, *SOIMUMPs Design Handbook, Revision 8.0*, MEMSCAP Inc., Durham, NC, USA, 2011.

[31] F. J. Giessibl, "Advances in atomic force microscopy," *Rev. Modern Phys.*, vol. 75, no. 3, pp. 949–983, Jul. 2003.

[32] M. Maroufi and S. O. Reza Moheimani, "Design, fabrication and characterization of a high-bandwidth 2DOF MEMS nanopositioner," in *Proc. IEEE/ASME Int. Conf. Adv. Intell. Mechatronics*, Wollongong, NSW, Australia, Jul. 2013, pp. 335–340.

[33] R. Frisch-Fay, *Flexible Bars*. London, U.K.: Butterworth, 1962.

[34] A. G. Fowler, A. Bazaei, and S. O. Reza Moheimani, "Design and analysis of nonuniformly shaped heaters for improved MEMS-based electrothermal displacement sensing," *J. Microelectromech. Syst.*, vol. 22, no. 3, pp. 687–694, Jun. 2013.

[35] A. Sebastian and D. Wiesmann, "Modeling and experimental identification of silicon microheater dynamics: A systems approach," *J. Microelectromech. Syst.*, vol. 17, no. 4, pp. 911–920, Aug. 2008.

[36] M. G. Ruppert and S. O. Reza Moheimani, "A novel self-sensing technique for tapping-mode atomic force microscopy," *Rev. Sci. Instrum.*, vol. 84, no. 12, p. 125006, 2013.

Mohammad Maroufi (S'14) received the B.Sc. degrees in mechanical engineering and applied physics as a Distinguished Student from the Amirkabir University of Technology (Tehran Polytechnic) in 2008, the master's degree in mechatronics from the Amirkabir University of Technology in 2011, and the Ph.D. degree in electrical engineering from the University of Newcastle, Australia. He is currently a Research Associate with the Department of Mechanical Engineering, University of Texas at Dallas. His research interests include the design and control of MEMS nanopositioning systems, MEMS-based sensing and actuation, on-chip atomic force microscopy, and modeling of smart materials and structures.

S. O. Reza Moheimani (F'11) currently holds the James von Ehr Distinguished Chair of Science and Technology with the Department of Mechanical Engineering, University of Texas at Dallas. His current research interests include ultrahigh-precision mechatronic systems, with a particular emphasis on dynamics and control at the nanometer scale, including applications of control and estimation in nanopositioning systems for high-speed scanning probe microscopy and nanomanufacturing, modeling and control of microcantilever-based devices, control of microactuators in microelectromechanical systems, and design, modeling and control of micromachined nanopositioners for on-chip scanning probe microscopy.

Dr. Moheimani is a Fellow of the International Federation of Automatic Control (IFAC) and the Institute of Physics, U.K. His research has been recognized with a number of awards including the IFAC Nathaniel B. Nichols Medal (2014), the IFAC Mechatronic Systems Award (2013), the IEEE Control Systems Technology Award (2009), the IEEE Transactions on Control Systems Technology Outstanding Paper Award (2007), and several best student paper awards in various conferences. He has served on the Editorial Boards of a number of journals, including the IEEE TRANSACTIONS ON MECHATRONICS, the IEEE TRANSACTIONS ON CONTROL SYSTEMS TECHNOLOGY, and *Control Engineering Practice*. He currently chairs the IFAC Technical Committee on Mechatronic Systems, and has chaired several international conferences and workshops. As of January 2016, he will assume the role of Editor-in-Chief of the *IFAC Mechatronics Journal*.